IJMF

Iranian Journal of Materials Forming

Research Article

Activation Energy and Zener-Hollomon Mapping of Hot-Deformed API X80 Steel Using Modified Hyperbolic Sine Constitutive Models

Hamed Eskandari, Mohsen Reihanian* and Seyed Reza Alavi Zaree

Department of Materials Science and Engineering, Faculty of Engineering, Shahid Chamran University of Ahvaz, Ahvaz, Iran

ARTICLE INFO	ABSTRACT
	This study investigates the hot deformation behavior of API X80 pipeline steel using modified hyperbolic sine-based constitutive models. Uniaxial compression tests were conducted at temperatures of 950 to 1100 °C and strain rates of 0.001 to 1 s⁻¹. Five constitutive approaches were evaluated: linear-linear Shi (LLS), linear-polynomial Shi (LPS), polynomial-polynomial Shi (PPS), and polynomial-polynomial Yang (PPY). Results indicate that activation energy (Q) varies significantly with deformation conditions. While the constant Q (CAE) model provides reasonable predictive accuracy and remains useful for simplified analysis, the PPY model demonstrates superior performance by capturing complex dependencies between stress, temperature, and strain rate. Zener-Hollomon (Z) maps and Q contours further illustrate the impact of model selection on process prediction. These findings establish a reliable computational framework for accurately modeling and optimizing hot deformation in high-strength steels.
	© Shiraz University, Shiraz, Iran, 2025

1. Introduction

Determining anteversion energy (Q) accurately is crucial for understanding hot deformation behavior, optimizing processing parameters, and predicting material responses under varying conditions [1-3]. Traditional models often assume a constant Q (CAE), which fails to account for its variability across different deformation scenarios. To address this, researchers have modified constitutive equations to incorporate the effects of temperature and strain rate on Q. The hyperbolic-sine equation, widely used for modeling flow stress behavior, effectively links strain rate, temperature, and flow stress [4]. However, conventional models often overlook the variability in parameters like Q, potentially leading to

less accurate predictions of material behavior under diverse processing conditions.

Shi et al. [5, 6] developed a modified version of the original constitutive equation [4] to account for the effects of deformation temperature and strain rate on Q, initially applied to 7150 aluminum alloys. Subsequent studies extended this approach to other materials, such as Son et al.'s mapping of Q and microstructural effects in AA5052 alloy [7], Sun et al.'s application to TiAl-based alloys [8], and Zhao et al.'s assessment of Ti-5Al-5V-5Mo-3Cr alloys [9]. The modified model has also been effectively used to study Ti-15-3 titanium alloy [10], super-304H stainless steel [11] and Inconel 740 nickel-based superalloys [12]. Yang et al. [13] further advanced the model by deriving partial equations that include previously neglected terms, enhancing its accuracy and applicability.

Recent studies have used machine learning (ML) and artificial neural network (ANN) to model the hot deformation of pipeline steels. Fangpo et al. [14] applied ANN to high-strength offshore steel, showing it outperformed the Arrhenius model. Abarghooei et al. [15] used a genetic algorithm to optimize steady-state hot-flow modeling parameters for API X70 steel. Ahmadi et al. [16] found ANN most effective for predicting complex deformation behaviors, including multi-peak flow due to dynamic recrystallization (DRX). In addition to ML and ANN approaches, extensive research has been conducted on the hot deformation behavior of various pipeline steels. However, studies specifically targeting API X80 steel remain scarce. Research on API X80 steel has explored various aspects of its hot deformation behavior. Qiao et al. [17] investigated the effects of Nb and C content, finding that increasing Nb from 0.082% to 0.13% (mass fraction) raised the recrystallization Q from 387 to 481 kJ/mol, while the ratio of Nb/C also played a significant role. Gomez et al. [18] simulated hot rolling and analyzed the evolution of austenite microstructure and precipitation, observing that finer, more equiaxed ferrite grains resulted from more severe austenite deformation. Shen et al. [19] conducted hot compression tests, establishing constitutive equations and kinetic models for DRX, and

found that the hot deformation Q of X80 steel is higher than that of C-Mn and low-carbon steel. Mendes-Fonseca et al. [20] studied dynamic transformation during simulated hot rolling, concluding it was mechanically activated and occurred under all conditions, with the volume fraction of retained ferrite increasing with retained strain. Eskandari et al. [21, 22] also contributed to the field by modeling material flow curves and analyzing the efficiency parameter used for developing processing maps.

While the above-mentioned studies address specific features of X80 steel, a gap remains in the literature regarding a comprehensive evaluation of Q and Zener-Hollomon (Z) parameter distributions using different modified hyperbolic-sine constitutive models. This study addresses that gap by employing modified hyperbolic-sine constitutive models, incorporating innovations proposed by Shi et al. [5, 6] and Yang et al. [13]. In addition, it introduces a novel Q map developed through advanced regression techniques, offering new insights into the material's hot deformation behavior. By integrating predictive modeling with microstructural analysis, the research establishes a robust framework for understanding the interplay between Q and microstructural evolution. These advancements provide a more accurate foundation for optimizing processing parameters and improving the performance of API X80 steel in practical applications.

2. Materials and Method

The chemical composition of the API X80 steel used in this study was previously reported [21]. Cylindrical compression samples, 10 mm in height and 7 mm in diameter, were cut from rolled plates with the axis parallel to the rolling direction. Compression tests were performed on a Zwick Z250 machine with a maximum load capacity of 250 kN. Samples were heated to 1200 °C for 10 minutes, cooled to the desired deformation temperature and held for 5 minutes. A variety of strain rates (0.001, 0.01, 0.1, and 1 s⁻¹) and temperatures (950, 1000, 1050, and 1100 °C) were applied to achieve a true strain of 0.7. Graphite sheets were used as a lubricant. The samples were progressively ground with SiC

abrasive paper, mechanically polished, and etched with 4% Picral reagent to reveal prior austenite grain boundaries. A 2% Nital etch was used to identify phase constituents. The microstructures were examined using an optical microscope.

3. Modified Hyperbolic Sine Constitutive Models

The original hyperbolic-sine equation is used to represent the correlation between strain rate, deformation temperature, and flow stress [4]:

$$\ln \dot{\varepsilon} = \ln A + n \ln[\sinh(\alpha\sigma_p)] - \frac{Q}{RT} \quad (1)$$

Where n and A are material constants, α is a stress multiplier, σ_p is the peak flow stress, Q is activation energy for hot deformation, R is the universal gas constant, and T is the deformation temperature. The stress multiplier α can be defined as $\alpha = \beta/n_1$, where β and n_1 are determined from the slopes of the $\ln(\dot{\varepsilon})$ vs. σ_p and $\ln(\dot{\varepsilon})$ vs. $\ln(\sigma_p)$ plots, respectively, within the investigated temperature range. The original constitutive equation, upon partial differentiation, reveals a constant Q independent of both temperature and strain rate, as defined by:

$$Q = RnS \quad (2)$$

Here, n represents the average slope of the $\ln(\dot{\varepsilon})$ vs. $ln[sinh(\alpha\sigma_p)]$ plots at various temperatures, while S is the average slope of the $ln[sinh(\alpha\sigma_p)]$ vs. $1/T$ plots at different strain rates.

When n and Q are evaluated as functions of deformation parameters, Eq. (1) becomes:

$$\ln \dot{\varepsilon} = \ln A + n(T) \ln[\sinh(\alpha\sigma_p)] - \frac{Q(\dot{\varepsilon},T)}{RT} \quad (3)$$

Taking the partial derivatives of the reciprocal of temperature on both sides of Eq. (3) yields [5, 13]:

$$Q(\dot{\varepsilon},T) = R \frac{\partial n(T)}{\partial\left(\frac{1}{T}\right)} \ln[\sinh(\alpha\sigma_p)] +$$
$$Rn(T) \frac{\partial \ln[\sinh(\alpha\sigma_p)]}{\partial\left(\frac{1}{T}\right)} - \frac{\partial Q(\dot{\varepsilon},T)}{T\partial\left(\frac{1}{T}\right)} \quad (4)$$

Shi et al. [5, 6] modified the original model to include

temperature-dependent n through linear regression and strain rate-influenced S via polynomial regression, proposing a temperature and strain rate dependence of Q as follows:

$$Q(T,\dot{\varepsilon}) = Rn(T)S(\dot{\varepsilon}) \quad (5)$$

Yang et al. [13] revised the partial equations to enhance accuracy under various deformation conditions and introduced the subsequent equation:

$$\ln[sinh(\alpha\sigma_p)] = \frac{S(\ln \dot{\varepsilon})}{T} + f(\ln \dot{\varepsilon}) \quad (6)$$

Polynomial regression was employed to determine the precise functional forms of $n(T)$, $S(\ln \dot{\varepsilon})$, and $f(\ln \dot{\varepsilon})$. This allows for the determination of each term in the modified Arrhenius equations, leading to the calculation of Q using the Eq. (7):

$$Q(T,\dot{\varepsilon}) = RT\ln A + RTn(T) \ln[sinh(\alpha\sigma_p)] - RT\ln \dot{\varepsilon} \quad (7)$$

While the CAE model assumes a constant Q for all deformation conditions, this simplification may not hold outside the experimental range because the apparent Q is determined by the free energy barrier for dislocation motion, which varies with temperature, applied stress, and microstructure. In the Shi-based approaches, only the second term of Eq. (4) is calculated, while the first and third terms are neglected, which may lead to non-negligible errors when extrapolated. Furthermore, the logarithmic form of these models requires solving a partial differential equation for accurate Q determination, adding complexity and potential uncertainty. Yang's modification addresses these issues by retaining all relevant terms, thereby improving the accuracy and reliability of peak stress analysis. Nevertheless, when Q varies significantly, the traditional Z parameter may lose its physical meaning, and a modified form, as proposed in Yang's work, should be adopted for predictions beyond the tested deformation range.

This study investigates the hot deformation behavior of API X80 steel using a set of constitutive models, including the traditional constant Q (CAE) model and

several modified approaches. The linear-linear Shi (LLS), linear-polynomial Shi (LPS), and polynomial-polynomial Shi (PPS) models employ Eq. (5) with varying combinations of linear and polynomial regressions for *n* and *S*, while the polynomial-polynomial Yang (PPY) model applies Eq. (7) with polynomial fits for the relevant parameters. A key advantage of these models is the simplification of the pre-exponential factor (*A*), which becomes independent of deformation conditions. By conducting these comparative analyses, the study seeks to provide a more comprehensive understanding of the hot deformation behavior of X80 steel under diverse processing conditions.

4. Results and Discussion

4.1. Compressive stress-strain curves analysis

Fig. 1 illustrates the stress-strain behavior of X80 steel at various temperatures and strain rates. At lower temperatures and higher strain rates, the material exhibits continuous work hardening without a distinct peak stress, indicating that dynamic recovery (DRV) dominates over dynamic recrystallization (DRX). As the temperature increases, a peak stress appears at lower strain rates, signifying the onset of DRX. With further increase in temperature, peak stress emerges even at higher strain rates, suggesting enhanced DRX activity. These observations demonstrate that both temperature and strain rate significantly influence the deformation mechanisms in X80 steel.

The values of the parameters *n* and *S*, determined through linear regression, are not constant but vary with deformation conditions such as temperature and strain rate. Averaging these values can be misleading because of their dependence on these factors. Fig. 2 illustrates this dependence, showing how *n* and *S* change with temperature and strain rate, respectively. The relationships between these parameters and deformation conditions can be modeled using both linear and polynomial functions. To derive the exact form of the function $f(\ln \dot{\varepsilon})$, polynomial fits for *n* and *S* are considered.
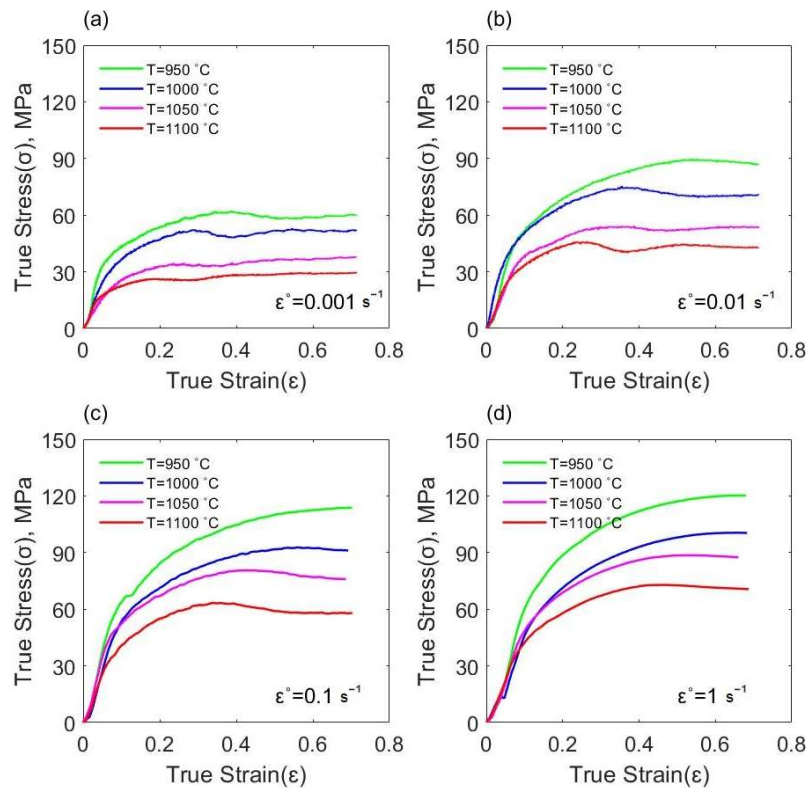

Fig. 1. Flow stress curves of API X80 steel obtained at temperatures ranging from 950 ºC to 1100 ºC and strain rates of (a) 0.001 s⁻¹, (b) 0.01 s⁻¹, (c) 0.1 s⁻¹, and (d) 1 s⁻¹.
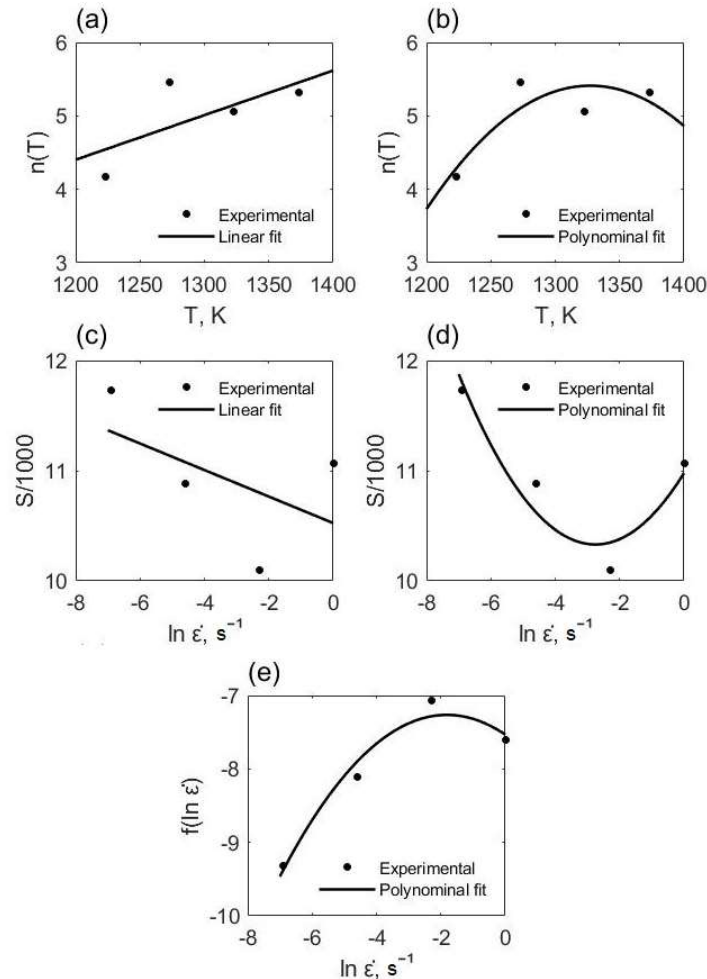
Fig. 2. Experimental relationship between deformation parameters and temperature or strain rate: (a) linear fit of *n* as a function of temperature, (b) Polynomial fit of *n*, (c) linear fit of *S* plotted against the $\ln \dot{\varepsilon}$, (d) polynomial fit of *S* against $ln\dot{\varepsilon}$, and (e) polynomial fit of $f(\ln \dot{\varepsilon})$ against $\ln \dot{\varepsilon}$.

4.2. Activation energy and Zener-Hollomon map

Fig. 3 illustrates *Q* maps generated by four modeling approaches (LLS, LPS, PPS, and PPY) for hot deformation, showing how *Q* changes with temperature and strain rate. The LLS approach provides a simple, linear representation. The LPS model introduces non-linearity, capturing more nuanced behavior with gradual *Q* decreases. The PPS approach produces a highly intricate map, revealing complex dependencies on temperature and strain rate with sharper transitions, suggesting significant sensitivity to both parameters. Finally, the PPY approach further refines the predictions, emphasizing specific behaviors that align more closely with physical phenomena observed during hot deformation. Overall, the complexity of the *Q* maps

increases with the sophistication of the modeling approach, progressing from simple linear relationships to detailed maps that capture the nuanced interactions between temperature and strain rate.

The *Q* range also differs considerably between approaches: LLS shows the widest spread (400–540 kJ mol⁻¹), followed by LPS (400–580 kJ mol⁻¹) and PPS (380–540 kJ mol⁻¹), while PPY yields the narrowest range (435–460 kJ mol⁻¹). The relatively confined range of *Q* indicates PPY lower sensitivity to experimental scatter and stronger correlation with observed microstructural changes. Moreover, the PPY map reveals a stable high-*Q* region (~460 kJ mol⁻¹) concentrated at moderate strain rates and higher temperatures, conditions corresponding to DRX and
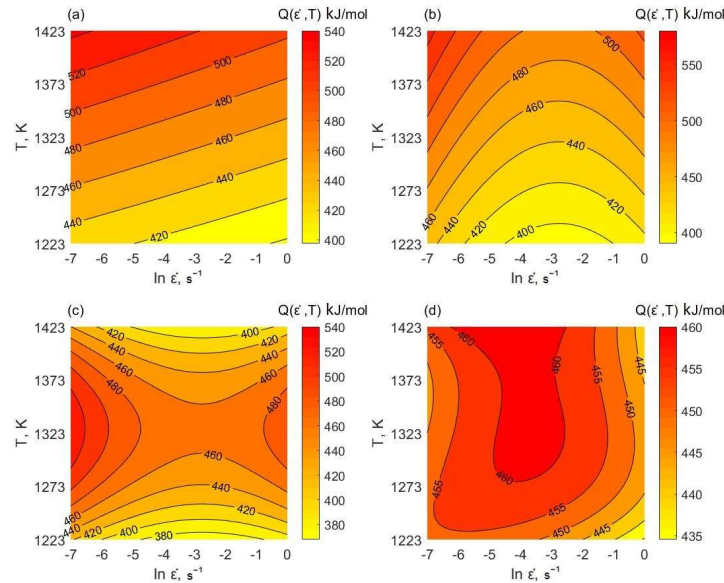
Fig. 3. *Q* maps generated using the (a) LLS, (b) LPS, (c) PPS, and (d) PPY approaches.

fine-grained microstructures. By contrast, the LLS, LPS, and PPS maps display broader *Q* variations with less localized high-*Q* domains, making the optimal processing region less distinct.

Several studies on X80 and related pipeline steels report hot-deformation or recrystallization activation energies spanning a broad range, depending on composition and the specific process analyzed. For example, Qiao et al. [17] reported that increasing Nb content from 0.05 % to 0.12 % (mass fraction) raised *Q* from ~387 to ~481 kJ·mol⁻¹. Niu et al. [23] found DRX activation energies of ~365–395 kJ·mol⁻¹ for high-grade X80/X100 steels with varying Nb levels. Liu et al. [24] reported SRX and deformation activation energies of ~366 kJ·mol⁻¹ and ~393 kJ·mol⁻¹, respectively, for untreated X80 steel (without RE additions). In related microalloyed pipeline steels, Wang et al. [25] obtained ~358 kJ·mol⁻¹. These prior results fall broadly within the same range as the present PPY-derived *Q* values (~435–460 kJ·mol⁻¹), though our values are somewhat higher. The differences can be attributed to variations in chemical composition, whether *Q* was determined for SRX, DRX, or overall hot deformation, and the modeling method (constant-*Q* vs. variable-*Q*). In particular, variable-*Q* approaches, such as the PPY model account for mechanism transitions and microstructural evolution, typically yielding higher

mechanism-sensitive activation energies than constant-*Q* fits.

While all the presented maps aim to illuminate the deformation landscape, their varying levels of complexity highlight the importance of choosing the appropriate model based on material behavior and deformation mechanisms. Factors such as DRX, grain size distribution, phase transformations, dislocation density, and texture can significantly influence *Q*, leading to deviations from theoretical predictions. For instance, hard phases may impede dislocation motion, requiring higher *Q*, while variations in dislocation density can obscure expected linear relationships.

This study emphasizes that the chosen mathematical approach plays a crucial role in accurately characterizing *Q* profiles, revealing the complexity of material behavior and the potential discrepancies between experimental results and theoretical models.

It should be noted that the *Q* values reported here represent apparent activation energies derived directly from experimental flow curves without prior normalization of stress by the temperature-dependent Young's modulus or of strain rate by the self-diffusion rate. This approach was intentionally adopted to capture the practical variation of *Q* under industrially relevant hot-working conditions, where deformation mechanisms can shift between DRV, DRX, or mixed modes

depending on temperature, strain rate, and strain. By contrast, when deformation occurs under a single mechanism and the data are normalized as suggested by Sellars and McTegart [4], the Q typically collapses to a constant value close to the self-diffusion Q of the controlling species. Our microstructural observations (Section 4.4) confirm that different regions of the deformation map correspond to distinct microstructural states, explaining the observed variations in apparent Q. Therefore, the present findings do not contradict the physical basis of a constant intrinsic Q for a single mechanism, but rather reflect the influence of mechanism transitions and evolving microstructure on the experimentally derived values.

Fig. 4 presents $\ln Z$ maps illustrating the effects of different Q estimation approaches on material flow behavior. The CAE approach produces uniform contours and a limited Z value range, potentially overlooking nuanced material responses. The LLS approach yields smoother contours with a slightly narrower Z range. The LPS approach introduces greater variability in Z values, while the PPS approach, with polynomial fits for both parameters, exhibits the most pronounced fluctuations.

Finally, the PPY approach generates a Z value range similar to the CAE model. These maps demonstrate how the choice of Q estimation method significantly influences the predicted material flow behavior across various temperatures and strain rates.

In the $\ln Z$ maps, the CAE model shows a contour range of ~32–44, while the other approaches present slightly broader ranges: LLS (35–42), LPS (35–44), PPS (30–45), and PPY (32–42). Although the PPY approach does not yield the narrowest $\ln Z$ range, it provides smoother and more coherent contour patterns, enabling clearer identification of a DRX-favorable window at ~1050–1100 °C and strain rates of 0.01–0.1 s^{-1}. This domain is characterized by stable, high Q values and moderate $\ln Z$, consistent with microstructural evidence of uniform fine grains (see following sections). Overall, while other approaches produce more scattered or diffuse high-Q and moderate-$\ln Z$ regions, the PPY model offers the most consistent overlap between Q, $\ln Z$, and microstructural observations, making it the most effective for defining an industrially relevant processing window.

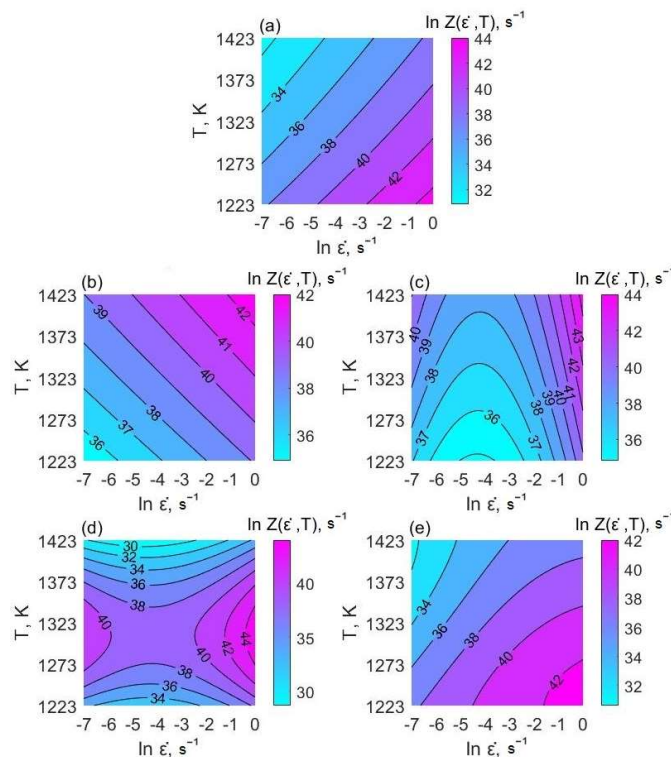Traditional models often assume constant Q, leading

Fig. 4. $\ln Z$ maps generated using the (a) CAE (b) LLS, (c) LPS, (d) PPS, and (e) PPY approaches.

to a straightforward relationship in which Z increases with decreasing temperature and increasing strain rate. However, when Q varies with temperature and strain rate, this simple relationship becomes more complex. For example, a significant increase in Q at higher temperatures can offset the expected decrease in Z due to temperature, altering the predicted trend. Microstructural features such as grain size and dislocation density further complicate this relationship, producing Z variations that deviate from theoretical predictions. Consequently, materials may exhibit unexpected flow behavior during hot deformation, underscoring the need to account for these complex interactions to accurately model and predict industrial processing behavior.

4.3. Approach validation and comparison

The effectiveness of the approaches was evaluated by analyzing the linearity of the $\ln Z - \ln[\sinh(\alpha\sigma_p)]$ plots, as predicted by the Arrhenius constitutive equation. The results (Fig. 5) revealed varying degrees of linearity across the different modeling approaches. The CAE model demonstrates the strongest linearity, suggesting that treating parameters as constants can be an effective simplification in certain cases. By contrast, the LLS, LPS, and PPS approaches exhibit poor linearity, indicating that simpler linear or polynomial fits are inadequate for capturing the complex behavior. The PPY approach, however, shows improved linearity, demonstrating that more sophisticated modeling techniques are necessary to accurately represent the hot deformation characteristics of X80 steel. This analysis highlights the limitations of simpler models and reinforces the importance of advanced methodologies in material deformation studies.

The accuracy of the proposed constitutive models was evaluated by comparing predicted peak stresses with experimental data, as shown in Fig. 6. The CAE approach, which assumes constant parameters, showed reasonable correlation. In contrast, the LLS approach, employing linear fits for both n and S, exhibited significantly lower accuracy. The LPS approach, which combines a linear fit for n and a polynomial fit for S,

demonstrated poor correlation, underscoring the limitations of applying linear assumptions to n. The PPS approach, using polynomial fits for both parameters, showed some improvement over LPS but still exhibited notable deviations. By comparison, the PPY approach, incorporating the Yang modification, achieved good correlation with experimental data. Ultimately, the choice of the optimal approach depends on the specific application and the required level of accuracy.

As shown by the correlation coefficients (R) provided directly in Figs. 5 and 6, a clear Quantitative comparison of the predictive capabilities of the different constitutive models can be made. In the linearity assessment (Fig. 5), the CAE model yields $R = 0.9767$, while the other approaches show markedly different performance: LLS ($R = 0.2442$), LPS ($R = -0.0948$), PPS ($R = 0.0502$), and PPY ($R = 0.9936$). Similarly, for the peak stress prediction accuracy (Fig. 6), the R values are: CAE (0.9695), LLS (0.2898), LPS (–0.0332), PPS (0.1008), and PPY (0.9949). These results clearly indicate that the PPY model achieves the highest correlation with experimental data in both evaluations, outperforming all other models and even slightly surpassing the CAE model. This agreement between PPY predictions and experimental results provides strong statistical support for selecting the PPY approach as the most accurate and reliable model for representing the hot deformation behavior of API X80 steel.

The LLS, LPS, and PPS approaches, which proved effective for materials such as aluminum alloys [5, 6], did not yield satisfactory results for X80 steel, suggesting that these models may not fully capture the complex deformation mechanisms specific to this material. The accuracy of any approach is influenced by factors such as the quality and quantity of experimental data, the intrinsic material behavior, and the range of deformation conditions considered. Therefore, the suitability of a particular approach depends strongly on the specific material system and deformation window of interest. Further research and refinement, including the exploration of more complex functional forms and the incorporation of additional material parameters, may be required to improve the accuracy and reliability of
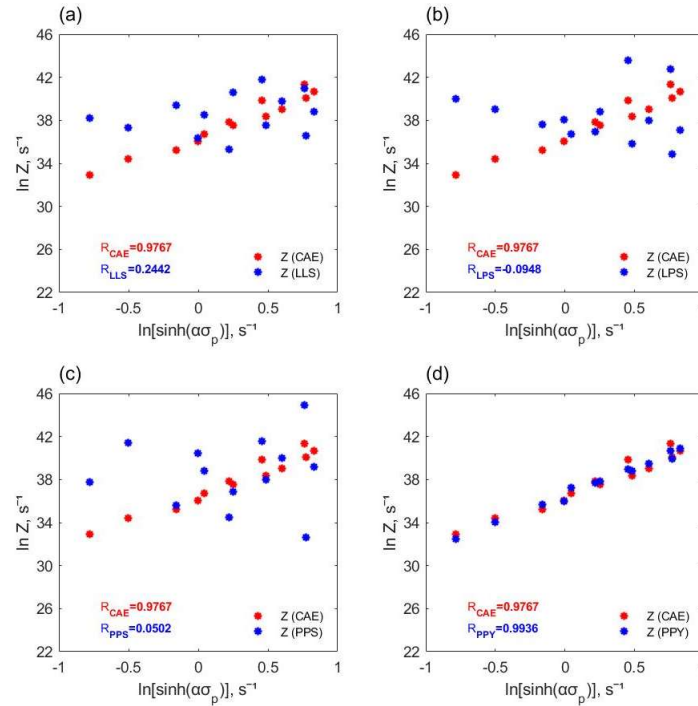
Fig. 5. Comparison of $\ln Z - \ln[sinh(\alpha\sigma_p)]$ plot derived from various approaches: (a) LLS vs. CAE, (b) LPS vs. CAE, (c) PPS vs. CAE, and (d) PPY vs. CAE.
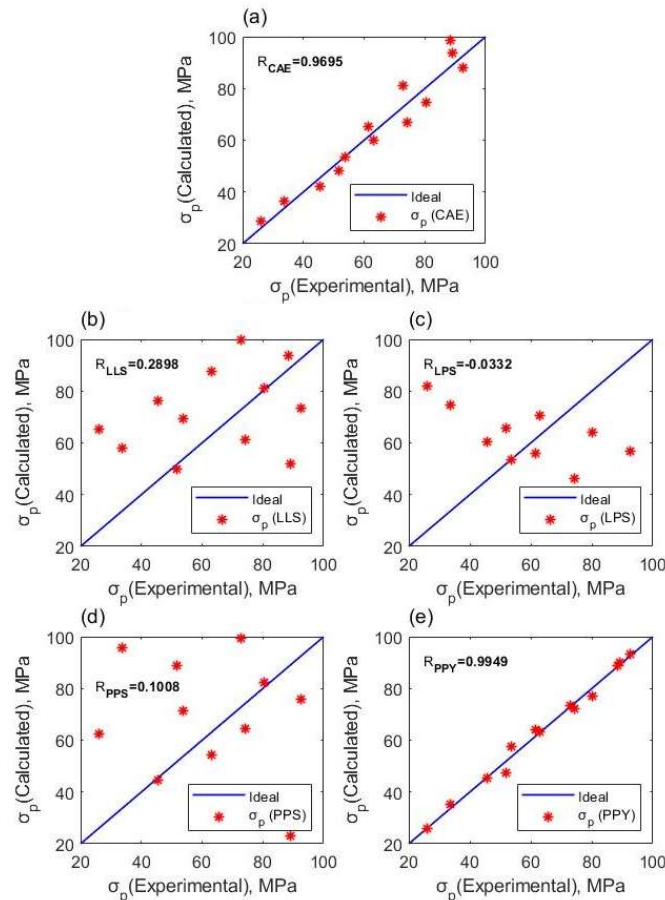

Fig. 6. Experimental peak stresses compared with calculated values based on (a) CAE, (b) LLS, (c) LPS, (d) PPS, and (e) PPY.

constitutive models for practical applications.

4.4. Microstructural observations

Fig. 7 illustrates the optical microstructures of API X80 steel deformed at 1050 °C under different strain rates. At lower strain rates of 0.001 s⁻¹ (a) and 0.01 s⁻¹ (b), the microstructures exhibit relatively large, less distinct grains, and prior austenite grain boundaries are not clearly visible. This can be attributed to limited grain refinement and less pronounced DRX under slow deformation conditions. As the strain rate increases to 0.1 s⁻¹ (c), the grain size becomes noticeably smaller and more uniform, with clearer definition of prior austenite grain boundaries. At the highest strain rate of 1 s⁻¹ (d), the microstructure shows the finest and most uniform grains, with even more distinct prior austenite boundaries. This enhanced refinement and visibility result from accelerated DRX and suppressed grain growth under rapid deformation. These results confirm that increasing strain rate significantly promotes grain refinement and improves the delineation of prior austenite grain boundaries in API X80 steel during hot deformation.

The optical microstructures of X80 steel (etching with Nital 2%), subjected to hot deformation at 1050 °C under different strain rates, are depicted in Fig. 8. After etching with Nital 2%, the microstructure exhibited regions of varying brightness and darkness, corresponding to different phases. The likely phases present in X80 steel include ferrite, pearlite, bainite, and residual austenite. The brighter regions are likely ferrite or residual austenite, while the darker regions correspond to bainite. Various studies have reported different microstructural types in X80 steel, including acicular ferrite, bainitic ferrite, degenerate martensite/austenite, and a ferritic matrix with dispersed martensite-austenite particles [26-29]. These variations arise primarily from differences in processing methods and cooling rates.

The Q for hot deformation is influenced by both temperature and strain rate. Lower temperatures and higher strain rates necessitate higher activation energies for dislocation movement, while higher temperatures and lower strain rates reduce the required Q. An increase in Q is often associated with more complete recrystallization or the formation of finer-grained microstructures. The observed microstructures in Fig. 7 and 8 align with these trends, with higher strain rates leading to finer grains and higher activation energies, and lower strain rates promoting DRX and lower activation energies. Understanding the interplay between temperature, strain rate, and Q is crucial for optimizing hot deformation processes to achieve desired microstructures and mechanical properties.

Literature reports [8, 10] have shown that domains exhibiting a nearly constant and relatively high Q can be regarded as potential optimal processing windows.

In this study, comparison of the Q and $\ln Z$ maps (Figs. 3 and 4) reveals that Q varies significantly among the constitutive approaches: LLS (400–540 kJ mol⁻¹), LPS (400–580 kJ mol⁻¹), PPS (380–540 kJ mol⁻¹), and PPY (435–460 kJ mol⁻¹). The PPY approach produces the narrowest Q range, indicating reduced sensitivity to experimental scatter and better alignment with microstructural observations. A stable high-Q region (~460 kJ mol⁻¹) is concentrated at ~1050–1100 °C and strain rates of 0.01–0.1 s⁻¹, matching the DRX-favorable microstructures shown in Figs. 7(c) and 7(d).

For the $\ln Z$ maps, the CAE model exhibits a range of ~32–44, while the other approaches show: LLS (35–42), LPS (35–44), PPS (30–45), and PPY (32–42). Although PPY does not have the narrowest $\ln Z$ range, its map shows smoother contours and a more distinct overlap between the high-Q region and moderate $\ln Z$ values, facilitating clear identification of an optimal processing domain. Outside this range, Q values decrease and DRV becomes the dominant mechanism, resulting in coarser grains and higher flow stresses. These findings confirm that integrating Q mapping with $\ln Z$ analysis provides a robust tool for identifying safe and effective hot-working schedules for API X80 steel.
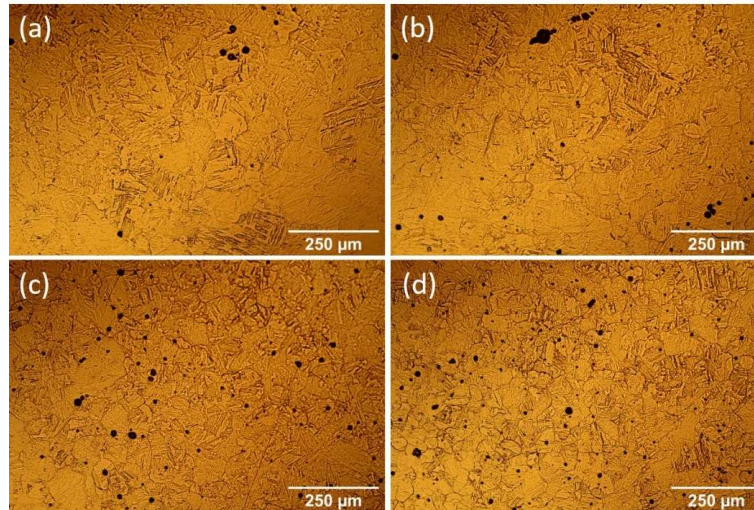
Fig. 7. Optical microstructure of X80 steel (Picral etch) deformed at 1050 °C and strain rates of (a) 0.001, (b) 0.01, (c) 0.1, and (d) 1 s⁻¹. The micrographs were taken perpendicular to the compression axis.

Fig. 8. Optical microstructure of X80 steel (Nital etch) deformed at 1050 °C and strain rates of (a) 0.001, (b) 0.01, (c) 0.1, and (d) 1 s⁻¹. The micrographs were taken perpendicular to the compression axis.
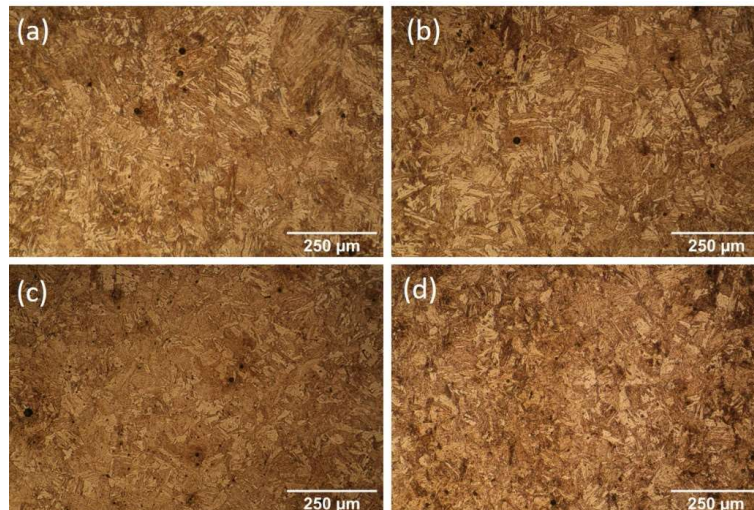
5. Conclusions

This study investigated the hot deformation behavior of API X80 pipeline steel using a series of modified hyperbolic sine constitutive models. Based on experimental data and computational analysis, the following conclusions are drawn:

1. The activation energy for hot deformation is strongly dependent on both temperature and strain rate. Assuming a constant value, as in the CAE model, oversimplifies the material's behavior under complex deformation conditions.

2. Comparison between predicted and experimental peak stresses revealed that both the CAE and PPY models provided reasonable correlation. While the CAE model benefits from its simplicity, the PPY model, incorporating temperature- and strain rate-dependent polynomial functions, offers improved predictive accuracy and better alignment with microstructural features.

3. The Z parameter distributions derived from different models varied significantly, indicating that Q estimation strongly influence on predicted flow behavior under hot working conditions.

4. Microstructural observations confirmed the trend of grain refinement at higher strain rates and temperatures, consistent with Q and flow stress

predictions, particularly from the PPY model.

5. Although the CAE model remains a practical option for basic predictions, the PPY approach is more suitable for applications requiring detailed modeling of deformation behavior and process optimization in high-strength steels.

Authors' contributions

H. Eskandari: Investigation, Formal analysis, Validation

M. Reihanian: Supervision, Conceptualization, Writing original draft, Writing-review & editing

S. R. Alvai Zaree: Supervision

Conflict of interest

The authors have no relevant financial or non-financial interests to disclose.

Funding

6. References

[1] Sang, D., Fu, R., & Li, Y. (2016). The hot deformation activation energy of 7050 aluminum alloy under three different deformation modes. *Metals*, *6*(3), 49. https://doi.org/10.3390/met6030049

[2] Schindler, I., Kawulok, P., Očenášek, V., Opěla, P., Kawulok, R., & Rusz, S. (2019). Flow stress and hot deformation activation energy of 6082 aluminium alloy influenced by initial structural state. *Metals*, *9*(12), 1248. https://doi.org/10.3390/met9121248

[3] Momeni, A. (2016). The physical interpretation of the activation energy for hot deformation of Ni and Ni–30Cu alloys. *Journal of Materials Research*, *31*(8), 1077-1084. https://doi.org/10.1557/jmr.2016.81

[4] Sellars, C. M., & McTegart, W. J. (1966). On the mechanism of hot deformation. *Acta Metallurgica*, *14*(9), 1136-1138. https://doi.org/10.1016/0001-6160(66)90207-0

[5] Shi, C., Mao, W., & Chen, X.-G. (2013). Evolution of activation energy during hot deformation of AA7150 aluminum alloy. *Materials Science and Engineering: A*, *571*, 83-91. https://doi.org/10.1016/j.msea.2013.01.080

[6] Shi, C., & Chen, X.-G. (2016). Evolution of activation energies for hot deformation of 7150 aluminum alloys with various Zr and V additions. *Materials Science and Engineering: A*, *650*, 197-209. https://doi.org/10.1016/j.msea.2015.09.105

[7] Son, K. T., Kim, M. H., Kim, S. W., Lee, J. W., & Hyun, S. K. (2018). Evaluation of hot deformation characteristics in modified AA5052 using processing map and activation energy map under deformation heating. *Journal of Alloys and Compounds*, *740*, 96-108. https://doi.org/10.1016/j.jallcom.2017.12.357

[8] Sun, Y., Wan, Z., Hu, L., & Ren, J. (2015). Characterization of hot processing parameters of powder metallurgy TiAl-based alloy based on the activation energy map and processing map. *Materials & Design*, *86*, 922-932. https://doi.org/10.1016/j.matdes.2015.07.140

[9] Zhao, Q., Yang, F., Torrens, R., & Bolzoni, L. (2019). Comparison of hot deformation behaviour and microstructural evolution for Ti-5Al-5V-5Mo-3Cr alloys prepared by powder metallurgy and ingot metallurgy approaches. *Materials & Design*, *169*, 107682. https://doi.org/10.1016/j.matdes.2019.107682

[10] Zhang, J., Di, H., Wang, H., Mao, K., Ma, T., & Cao, Y. (2012). Hot deformation behavior of Ti-15-3 titanium alloy: a study using processing maps, activation energy map, and Zener–Hollomon parameter map. *Journal of Materials Science*, *47*(9), 4000-4011. https://doi.org/10.1007/s10853-012-6253-1

[11] Babu, K. A., Mozumder, Y. H., Saha, R., Sarma, V. S., & Mandal, S. (2018). Hot-workability of super-304H exhibiting continuous to discontinuous dynamic recrystallization transition. *Materials Science and Engineering: A*, *734*, 269-280. https://doi.org/10.1016/j.msea.2018.07.104

[12] Wang, M., Wang, W., Liu, Z., Sun, C., & Qian, L. (2018). Hot workability integrating processing and activation energy maps of Inconel 740 superalloy. *Materials Today Communications*, *14*, 188-198. https://doi.org/10.1016/j.mtcomm.2018.01.009

[13] Yang, P., Liu, C., Guo, Q., & Liu, Y. (2021). Variation of activation energy determined by a modified Arrhenius approach: Roles of dynamic recrystallization on the hot deformation of Ni-based superalloy. *Journal of Materials Science & Technology*, *72*, 162-171. https://doi.org/10.1016/j.jmst.2020.09.024

[14] Fangpo, L., Ning, L., Xiaojian, R., Song, Q., Caihong, L., Jianjun, W., Yang, X., & Bin, W. (2023). Arrhenius constitutive equation and artificial neural network model of flow stress in hot deformation of offshore steel with high strength and toughness. *Materials Technology*, *38*(1), 2264670. https://doi.org/10.1080/10667857.2023.2264670

[15] Abarghooei, H., Arabi, H., Seyedein, S. H., & Mirzakhani, B. (2017). Modeling of steady state hot flow behavior of API-X70 microalloyed steel using genetic

algorithm and design of experiments. *Applied Soft Computing*, *52*, 471-477. https://doi.org/10.1016/j.asoc.2016.10.021

[16] Ahmadi, H., Ashtiani, H. R., & Heidari, M. (2020). A comparative study of phenomenological, physically-based and artificial neural network models to predict the Hot flow behavior of API 5CT-L80 steel. *Materials Today Communications*, *25*, 101528. https://doi.org/10.1016/j.mtcomm.2020.101528

[17] Qiao, G. Y., Xiao, F. R., Zhang, X. B., Cao, Y. B., & Liao, B. (2009). Effects of contents of Nb and C on hot deformation behaviors of high Nb X80 pipeline steels. *Transactions of Nonferrous Metals Society of China*, *19*(6), 1395-1399. https://doi.org/10.1016/S1003-6326(09)60039-X

[18] Gomez, M., Valles, P., & Medina, S. F. (2011). Evolution of microstructure and precipitation state during thermomechanical processing of a X80 microalloyed steel. *Materials Science and Engineering: A*, *528*(13-14), 4761-4773. https://doi.org/10.1016/j.msea.2011.02.087

[19] Shen, W., Zhang, C., Zhang, L., Xu, Q., & Cui, Y. (2018). Experimental study on the hot deformation characterization of low-carbon Nb-V-Ti microalloyed steel. *Journal of Materials Engineering and Performance*, *27*, 4616-4624. https://doi.org/10.1007/s11665-018-3594-1

[20] Mendes-Fonseca, N., Rodrigues, S. F., Guo, B., & Jonas, J. J. (2019). Dynamic transformation during the simulated hot rolling of an API-X80 steel. *Steel Research International*, *90*(8), 1900091. https://doi.org/10.1002/srin.201900091

[21] Eskandari, H., Reihanian, M., & Zaree, S. A. (2024). Constitutive modeling, processing map optimization, and recrystallization kinetics of high-grade X80 pipeline steel. *Journal of Materials Research and Technology*, *33*, 2315-2330. https://doi.org/10.1016/j.jmrt.2024.09.217

[22] Eskandari, H., Reihanian, M., & Alavi Zaree, S. (2023). An analysis of efficiency parameter and its modifications utilized for development of processing maps. *Iranian Journal of Materials Forming*, *10*(4), 45-51. https://doi.org/10.22099/ijmf.2024.49537.1283

[23] Niu, T., Kang, Y. l., Gu, H. W., Yin, Y. Q., Qiao, M. L., & Jiang, J. X. (2010). Effect of Nb on the dynamic recrystallization behavior of high-grade pipeline steels. *International Journal of Minerals, Metallurgy, and Materials*, *17*(6), 742-747. https://doi.org/10.1007/s12613-010-0383-8

[24] Liu, H. L., Liu, C. J., & Jiang, M. F. (2010). Effects of rare earths on the austenite recrystallization behavior in X80 pipeline steel. *Advanced Materials Research*, *129-131*, 542-546.

https://doi.org/10.4028/www.scientific.net/AMR.129-131.542

[25] Wang, L., Ji, L., Yang, K., Gao, X., Chen, H., & Chi, Q. (2022). The flow stress–strain and dynamic recrystallization kinetics behavior of high-grade pipeline steels. *Materials*, *15*(20), 7356. https://doi.org/10.3390/ma15207356

[26] Zhao, J., Hu, W., Wang, X., Kang, J., Cao, Y., Yuan, G., Di, H., & Misra, R. (2016). A Novel thermo-mechanical controlled processing for large-thickness microalloyed 560 MPa (X80) pipeline strip under ultra-fast cooling. *Materials Science and Engineering: A*, *673*, 373-377. https://doi.org/10.1016/j.msea.2016.07.089

[27] Machado, F. R. d. S., Ferreira, J. C., Rodrigues, M. V. G., Lima, M. N. d. S., Loureiro, R. d. C. P., Siciliano, F., Silva, E. S., Reis, G. S., Sousa, R. C. d., & Aranas Jr, C. (2022). Dynamic ferrite formation and evolution above the Ae3 temperature during plate rolling simulation of an API X80 steel. *Metals*, *12*(8), 1239. https://doi.org/10.3390/met12081239

[28] Ma, G., Chen, Y., Wu, G., Wang, S., Li, T., Liu, W., Wu, H., Gao, J., Zhao, H., & Zhang, C. (2023). The effects of microalloying on the precipitation behavior and strength mechanisms of X80 high-strength pipeline steel under different processes. *Crystals*, *13*(5), 714. https://doi.org/10.3390/cryst13050714

[29] Silva, R. A., Pinto, A. L., Kuznetsov, A., & Bott, I. S. (2018). Precipitation and grain size effects on the tensile strain-hardening exponents of an API X80 steel pipe after high-frequency hot-induction bending. *Metals*, *8*(3), 168. https://doi.org/10.3390/met8030168